We are IntechOpen, the world's leading publisher of Open Access books Built by scientists, for scientists

4,800
Open access books available

122,000
International authors and editors

135M
Downloads

Our authors are among the

154
Countries delivered to

TOP 1%
most cited scientists

12.2%
Contributors from top 500 universities

WEB OF SCIENCE™

Selection of our books indexed in the Book Citation Index in Web of Science™ Core Collection (BKCI)

Interested in publishing with us?
Contact book.department@intechopen.com

Numbers displayed above are based on latest data collected.
For more information visit www.intechopen.com

Chapter 24

Piezomechanics in PZT Stack Actuators for Cryogenic Fuel Injectors

Yasuhide Shindo and Fumio Narita

Additional information is available at the end of the chapter

http://dx.doi.org/10.5772/50495

1. Introduction

Lead zirconate titanate (PZT) ceramics in special electronic devices such as structural health monitoring systems of liquid rocket engines and microvalves for space applications are subjected to cryogenic temperatures. PZT ceramics are also used in active fuel injectors under severe environments (Senousy et al. 2009a; 2009b). In the application of the PZT stack actuators to hydrogen fuel injectors, the actuators are operated under electric fields at cryogenic temperatures. Hence, it is important to understand the cryogenic electromechanical response of the PZT actuators under electric fields.

In this chapter, we address the present state of piezomechanics in PZT stack actuators for fuel injectors at cryogenic temperatures. First, we discuss the cryogenic response of PZT stack actuators under direct current (DC) electric fields (Shindo et al. 2011). A thermodynamic model is used to predict a monoclinic phase around a morphotropic phase boundary (MPB). A shift in the boundary between the tetragonal and rhombohedral/monoclinic phases with decreasing temperature is determined, and the temperature dependent piezoelectric coefficients are evaluated. Temperature dependent coercive electric field is also predicted based on the domain wall energy. A finite element analysis (FEA) is then performed, considering the shift in the MPB and polarization switching, to calculate the electromechanical fields of the PZT stack actuators from room to cryogenic temperatures. In addition, experimental results on the DC electric field induced strain, which verify the model, are presented. Next, we discuss the dynamic response of PZT stack actuators under alternating current (AC) electric fields at cryogenic temperatures (Shindo et al. 2012). Dynamic electromechanical fields of the PZT stack actuators from room to cryogenic temperatures are simulated by the FEA with MPB shift and domain wall motion effects. Dynamic strain measurements of the PZT stack actuators under AC electric fields are also presented, and a comparison is made between calculations and measurements to validate the predictions. Moreover, a parametric study using FEA is performed to

investigate the factors affecting the cryogenic response of PZT stack actuators and to provide a basis for selecting desirable design details.

2. Analysis

2.1. Basic equations

Consider the orthogonal coordinate system with axes x, y, and z. The Newton's second law (the equations of motion) and Gauss' law for piezoelectric materials are given by

$$\begin{aligned} \sigma_{xx,x} + \sigma_{yx,y} + \sigma_{zx,z} &= \rho u_{x,tt} \\ \sigma_{xy,x} + \sigma_{yy,y} + \sigma_{zy,z} &= \rho u_{y,tt} \\ \sigma_{xz,x} + \sigma_{yz,y} + \sigma_{zz,z} &= \rho u_{z,tt} \end{aligned} \tag{1}$$

$$D_{x,x} + D_{y,y} + D_{z,z} = 0 \tag{2}$$

where (σ_{xx}, σ_{yy}, σ_{zz}, $\sigma_{xy} = \sigma_{yx}$, $\sigma_{yz} = \sigma_{zy}$, $\sigma_{zx} = \sigma_{xz}$) and ($D_x$, D_y, D_z) are the components of stress tensor and electric displacement vector, (u_x, u_y, u_z) are the components of displacement vectors, ρ is the mass density, and a comma denotes partial differentiation with respect to the coordinates or the time t. Constitutive relations for PZT ceramics poled in the z-direction can be written as

$$\begin{Bmatrix} \varepsilon_{xx} \\ \varepsilon_{yy} \\ \varepsilon_{zz} \\ \varepsilon_{yz} \\ \varepsilon_{zx} \\ \varepsilon_{xy} \end{Bmatrix} = \begin{bmatrix} s_{11} & s_{12} & s_{13} & 0 & 0 & 0 \\ s_{12} & s_{11} & s_{13} & 0 & 0 & 0 \\ s_{13} & s_{13} & s_{33} & 0 & 0 & 0 \\ 0 & 0 & 0 & s_{44}/2 & 0 & 0 \\ 0 & 0 & 0 & 0 & s_{44}/2 & 0 \\ 0 & 0 & 0 & 0 & 0 & s_{66}/2 \end{bmatrix} \begin{Bmatrix} \sigma_{xx} \\ \sigma_{yy} \\ \sigma_{zz} \\ \sigma_{yz} \\ \sigma_{zx} \\ \sigma_{xy} \end{Bmatrix} + \begin{bmatrix} 0 & 0 & \bar{d}_{31} \\ 0 & 0 & \bar{d}_{31} \\ 0 & 0 & \bar{d}_{33} \\ 0 & \bar{d}_{15}/2 & 0 \\ \bar{d}_{15}/2 & 0 & 0 \\ 0 & 0 & 0 \end{bmatrix} \begin{Bmatrix} E_x \\ E_y \\ E_z \end{Bmatrix} + \begin{Bmatrix} \varepsilon^r_{xx} \\ \varepsilon^r_{yy} \\ \varepsilon^r_{zz} \\ \varepsilon^r_{yz} \\ \varepsilon^r_{zx} \\ \varepsilon^r_{xy} \end{Bmatrix} \tag{3}$$

$$\begin{Bmatrix} D_x \\ D_y \\ D_z \end{Bmatrix} = \begin{bmatrix} 0 & 0 & 0 & 0 & \bar{d}_{15} & 0 \\ 0 & 0 & 0 & \bar{d}_{15} & 0 & 0 \\ \bar{d}_{31} & \bar{d}_{31} & \bar{d}_{33} & 0 & 0 & 0 \end{bmatrix} \begin{Bmatrix} \sigma_{xx} \\ \sigma_{yy} \\ \sigma_{zz} \\ \sigma_{yz} \\ \sigma_{zx} \\ \sigma_{xy} \end{Bmatrix} + \begin{bmatrix} \in^{\mathrm{T}}_{11} & 0 & 0 \\ 0 & \in^{\mathrm{T}}_{11} & 0 \\ 0 & 0 & \in^{\mathrm{T}}_{33} \end{bmatrix} \begin{Bmatrix} E_x \\ E_y \\ E_z \end{Bmatrix} + \begin{Bmatrix} P^r_x \\ P^r_y \\ P^r_z \end{Bmatrix} \tag{4}$$

where (ε_{xx}, ε_{yy}, ε_{zz}, $\varepsilon_{xy} = \varepsilon_{yx}$, $\varepsilon_{yz} = \varepsilon_{zy}$, $\varepsilon_{zx} = \varepsilon_{xz}$) and ($E_x$, E_y, E_z) are the components of strain tensor and electric field intensity vector, ($\varepsilon_{xx}^r, \varepsilon_{yy}^r, \varepsilon_{zz}^r, \varepsilon_{xy}^r, \varepsilon_{yz}^r, \varepsilon_{zx}^r$) and (P_x^r, P_y^r, P_z^r) are the remanent strain and polarization components, (s_{11}, s_{12}, s_{13}, s_{33}, s_{44}, $s_{66} = 2(s_{11} - s_{12})$) are the elastic compliances, ($\bar{d}_{31}, \bar{d}_{33}, \bar{d}_{15}$) are the temperature dependent piezoelectric coefficients, and ($\in_{11}^{\mathrm{T}}, \in_{33}^{\mathrm{T}}$) are the dielectric constants. The quantities ε_{ij}^r and P_i^r are taken to be due entirely to polarization switching. The strain components are

$$\begin{aligned} &\varepsilon_{xx} = u_{x,x}, \qquad \varepsilon_{yy} = u_{y,y}, \qquad \varepsilon_{zz} = u_{z,z}, \\ &\varepsilon_{xy} = \frac{1}{2}\left(u_{x,y} + u_{y,x}\right), \qquad \varepsilon_{yz} = \frac{1}{2}\left(u_{y,z} + u_{z,y}\right), \qquad \varepsilon_{zx} = \frac{1}{2}\left(u_{z,x} + u_{x,z}\right) \end{aligned} \tag{5}$$

The electric field components are related to the electric potential ϕ by

$$E_x = -\phi_{,x}, \qquad E_y = -\phi_{,y}, \qquad E_z = -\phi_{,z} \tag{6}$$

2.2. Temperature dependent piezoelectric coefficient

Temperature dependent piezoelectric coefficient is outlined here. Figure 1 shows the phase diagram of PZT established in Jaffe et al. (1971) and Noheda et al. (2000). As the temperature T is lowered, PZT undergoes a paraelectric-to-ferroelectric phase transition, and the cubic unit cell is distorted depending on the mole fraction X of $PbTiO_3$. In the Zr-rich region, the paraelectric phase changes to orthorhombic phase. An intermediate monoclinic phase exists between the Zr-rich rhombohedral perovskite and Ti-rich tetragonal perovskite phases. Compositions between Zr/Ti ratios 90/10 and 65/35 reveals a ferroelectric-to-ferroelectric transition between rhombohedral space groups. This transition involves the oxygen octahedral tilt.

The MPB between the tetragonal and rhombohedral/monoclinic phases is the origin of the unusually high piezoelectric response of PZT, and this MPB is numerically predicted. For simplicity here, we ignore the octahedral tilt transition which differentiates the high temperature (HT) and low temperature (LT) rhombohedral phases, and the orthorhombic phase.

An energy function for the solid solution between the two end-members $PbTiO_3$ and $PbZrO_3$ is given by (Bell & Furman 2003)

$$\Delta G_{PZT} = XG_{PT}\left(p_i\right) + \left(1 - X\right)G_{PZ}\left(q_i\right) + G_C\left(p_i, q_i\right) \tag{7}$$

where p_i and q_i (i = 1,2,3) denote the polarizations of the $PbTiO_3$ and $PbZrO_3$, respectively, and

$$\begin{aligned} G_{PT}\left(p_i\right) &= 3.74\times10^5\left(T - T_{PT}\right)\left(p_1^2 + p_2^2 + p_3^2\right) - 7.9\times10^7\left(p_1^4 + p_2^4 + p_3^4\right) \\ &+7.5\times10^8\left(p_1^2p_2^2 + p_2^2p_3^2 + p_3^2p_1^2\right) + 2.61\times10^8\left(p_1^6 + p_2^6 + p_3^6\right) \\ &+6.3\times10^8\left\{p_1^4\left(p_2^2 + p_3^2\right) + p_2^4\left(p_3^2 + p_1^2\right) + p_3^4\left(p_1^2 + p_2^2\right)\right\} - 3.66\times10^9\,p_1^2p_2^2p_3^2 \end{aligned} \tag{8}$$

$$G_{PZ}(q_i) = 2.82\times10^5\left(T - T_{PZ}\right)\left(q_1^2 + q_2^2 + q_3^2\right) + 5.12\times10^8\left(q_1^4 + q_2^4 + q_3^4\right)$$
$$-6.5\times10^8\left(q_1^2q_2^2 + q_2^2q_3^2 + q_3^2q_1^2\right) + 5.93\times10^8\left(q_1^6 + q_2^6 + q_3^6\right) \quad (9)$$
$$+2\times10^9\left\{q_1^4\left(q_2^2 + q_3^2\right) + q_2^4\left(q_3^2 + q_1^2\right) + q_3^4\left(q_1^2 + q_2^2\right)\right\} - 9.5\times10^9 q_1^2q_2^2q_3^2$$

$$G_C(p_i, q_i) = \gamma_{200}\left(p_1^2q_1^2 + p_2^2q_2^2 + p_3^2q_3^2\right) + \gamma_{220}\left\{p_1^2\left(q_2^2 + q_3^2\right) + p_2^2\left(q_3^2 + q_1^2\right) + p_3^2\left(q_1^2 + q_2^2\right)\right\} \quad (10)$$

In Eqs. (8) - (10), G_{PT} and G_{PZ} are identical to a Landau-Devonshire potential (free energy of a ferroelectric crystal) up to sixth order, G_C represents the coupling energy, T_{PT} = 766 K and T_{PZ} = 503 K are the Curie temperatures of $PbTiO_3$ and $PbZrO_3$, respectively, and γ_{200} and γ_{220} are unknown coefficients.

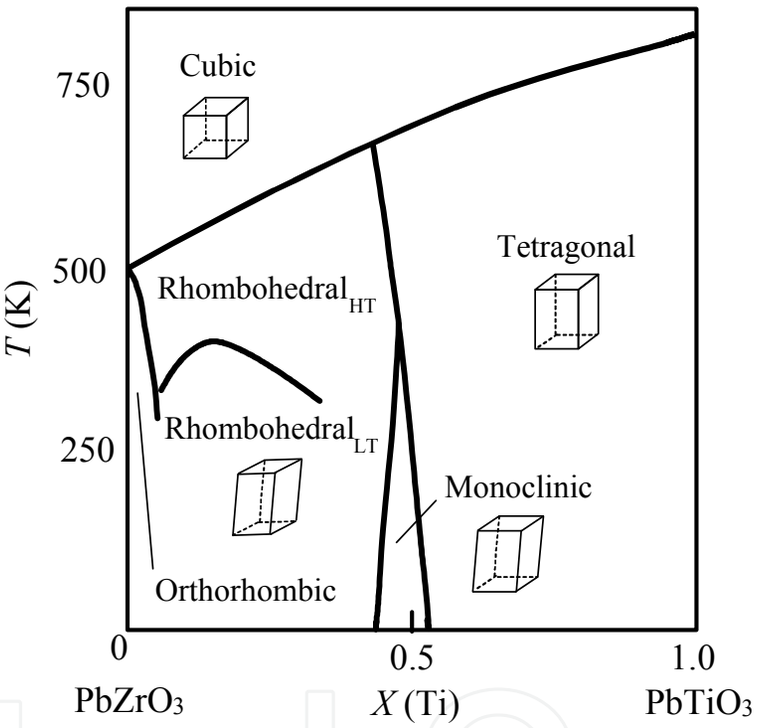

Figure 1. PZT phase diagram

The thermodynamic equilibrium state can be determined via minimization of ΔG_{PZT} with respect to p_i and q_i. For simplicity, only positive values of p_i and q_i are considered. For each temperature T and mole fraction X, the local minima in ΔG_{PZT} are systematically obtained for the following phases:

Cubic (C)

$$p_1 = p_2 = p_3 = 0, \qquad q_1 = q_2 = q_3 = 0 \quad (11)$$

Tetragonal (T)

$$p_1 = p_2 = 0, p_3 \neq 0, \qquad q_1 = q_2 = 0, q_3 \neq 0 \quad (12)$$

Rhombohedral (R)

$$p_1 = p_2 = p_3 \neq 0, \qquad q_1 = q_2 = q_3 \neq 0 \tag{13}$$

Monoclinic (M)

$$p_1 = p_2 \neq 0, p_3 \neq 0, \qquad q_1 = q_2 \neq 0, q_3 \neq 0 \tag{14}$$

The energies of the minima are then compared to define the stable state. In the simulation, $\gamma_{200} = 6\times10^8$ and $\gamma_{220} = 1.2\times10^8$ are assumed.

We now show a numerical example and comparison with experiments. Fig. 2 shows the

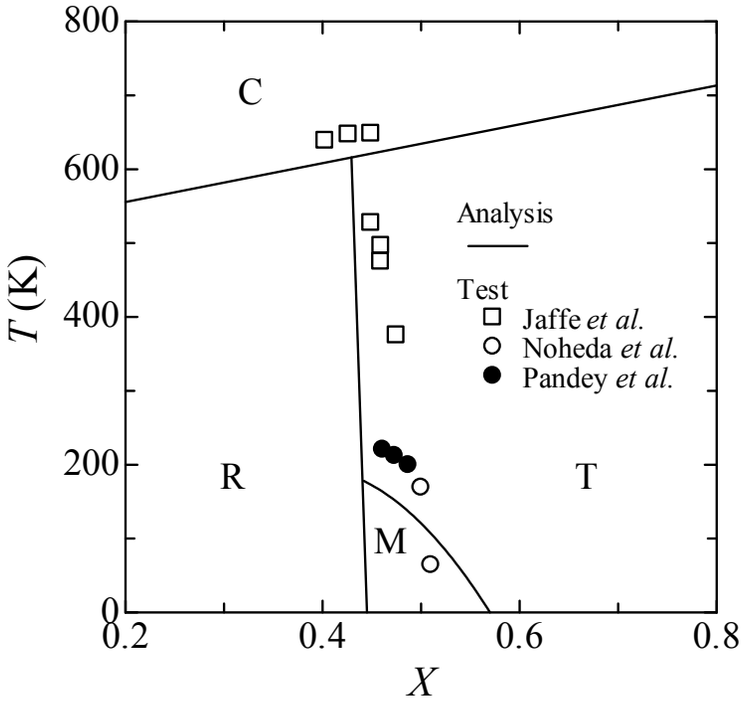

Figure 2. Calculated and experimental phase diagram of PZT

calculated PZT phase diagram. We also plot the experimental phase diagrams of PZT. The open square, open circle and solid circle are the results from Jeffe et al. (1971), Noheda et al. (2000) and Pandey et al. (2008). The simulation result reasonably agrees with the experimental data. It is noted that at room temperature, the MPB is located at about $X = 0.44$, and that there is an apparent shift of about 13 mol% in the MPB location on cooling to 0 K. In the work of Boucher et al. (2006), the piezoelectric coefficient d_{333} of PZT (Mn-doped) presented a significant decrease (about 85 %) due to a shift of 12 mol% of Zr at room temperature. Thus, from the consideration of Fig. 2, we propose the temperature dependent piezoelectric coefficient $\bar{d}_{ijk}$ ($\bar{d}_{311} = \bar{d}_{31}$, $\bar{d}_{333} = \bar{d}_{33}$, $\bar{d}_{131} = \bar{d}_{15}$ / 2 here) for $X = 0.44$, i.e.,

$$\bar{d}_{ijk} = \begin{cases} (1.7\times10^{-4}T + 0.95)d_{ijk} & 192 \le T \\ (1.0\times10^{-5}T^2 + 2.4\times10^{-3}T + 0.15)d_{ijk} & 0 < T \le 192 \end{cases} \tag{15}$$

where d_{ijk} ($d_{311}=d_{31}$, $d_{333}=d_{33}$, $d_{131}=d_{15}/2$ here) is the piezoelectric coefficient at 298 K. In Eqs. (3) and (4), reduced indices for the full notations of elastic compliances s_{ijkl} and temperature dependent piezoelectric coefficients $\bar{d}_{ijk}$ are used, with the following correspondence between the one and two indices: 1 = 11, 2 =22, 3 = 33, 4 = 23, 5 = 31, 6 = 12. We can also predict the piezoelectric coefficient for other mole fractions. For example, the temperature dependent piezoelectric coefficient for $X = 0.56$ can be expressed as

$$\bar{d}_{ijk} = \begin{cases} (-1.7\times10^{-4}T + 0.25)d_{ijk} & 192 \le T \\ (-1.0\times10^{-5}T^2 - 2.4\times10^{-3}T + 1.1)d_{ijk} & 20 < T \le 192 \\ (1.0\times10^{-5}T^2 + 2.4\times10^{-3}T + 0.95)d_{ijk} & 0 < T \le 20 \end{cases} \tag{16}$$

2.3. Polarization switching

High electromechanical fields lead to the polarization switching. We assume that the direction of a spontaneous polarization P^s of each grain can change by 180° or 90° for ferroelectric switching induced by a sufficiently large electric field opposite to the poling direction. The 90° ferroelastic domain switching is also induced by a sufficiently large stress field. The criterion states that a polarization switches when the electrical and mechanical work exceeds a critical value (Hwang et al. 1995)

$$\begin{aligned} &\sigma_{xx}\Delta\varepsilon_{xx} + \sigma_{yy}\Delta\varepsilon_{yy} + \sigma_{zz}\Delta\varepsilon_{zz} + 2\sigma_{xy}\Delta\varepsilon_{xy} + 2\sigma_{yz}\Delta\varepsilon_{yz} + 2\sigma_{zx}\Delta\varepsilon_{zx} \\ &+E_x\Delta P_x + E_y\Delta P_y + E_z\Delta P_z \ge 2P^s\bar{E}_c \end{aligned} \tag{17}$$

where $\bar{E}_c$ is a temperature dependent coercive electric field, and $\Delta\varepsilon_{ij}$ and ΔP_i are the changes in the spontaneous strain and polarization during switching, respectively. The values of $\Delta\varepsilon_{ij} = \varepsilon_{ij}^r$ and $\Delta P_i = P_i^r$ for 180° switching can be expressed as

$$\begin{aligned} &\Delta\varepsilon_{xx} = 0, \quad \Delta\varepsilon_{yy} = 0, \quad \Delta\varepsilon_{zz} = 0, \quad \Delta\varepsilon_{xy} = 0, \quad \Delta\varepsilon_{yz} = 0, \quad \Delta\varepsilon_{zx} = 0, \\ &\Delta P_x = 0, \quad \Delta P_y = 0, \quad \Delta P_z = -2P^s \end{aligned} \tag{18}$$

For 90° switching in the zx plane, the changes are

$$\begin{aligned} &\Delta\varepsilon_{xx} = \gamma^s, \quad \Delta\varepsilon_{yy} = 0, \quad \Delta\varepsilon_{zz} = -\gamma^s, \quad \Delta\varepsilon_{xy} = 0, \quad \Delta\varepsilon_{yz} = 0, \quad \Delta\varepsilon_{zx} = 0, \\ &\Delta P_x = \pm P^s, \quad \Delta P_y = 0, \quad \Delta P_z = -P^s \end{aligned} \tag{19}$$

where γ^s is a spontaneous strain. For 90° switching in the yz plane, we have

$$\begin{aligned} &\Delta\varepsilon_{xx} = 0, \quad \Delta\varepsilon_{yy} = \gamma^s, \quad \Delta\varepsilon_{zz} = -\gamma^s, \quad \Delta\varepsilon_{xy} = 0, \quad \Delta\varepsilon_{yz} = 0, \quad \Delta\varepsilon_{zx} = 0, \\ &\Delta P_x = 0, \quad \Delta P_y = \pm P^s, \quad \Delta P_z = -P^s \end{aligned} \tag{20}$$

The constitutive equations after polarization switching are

$$\begin{Bmatrix}\varepsilon_{xx}\\ \varepsilon_{yy}\\ \varepsilon_{zz}\\ \varepsilon_{yz}\\ \varepsilon_{zx}\\ \varepsilon_{xy}\end{Bmatrix}=\begin{bmatrix} s_{11} & s_{12} & s_{13} & 0 & 0 & 0\\ s_{12} & s_{11} & s_{13} & 0 & 0 & 0\\ s_{13} & s_{13} & s_{33} & 0 & 0 & 0\\ 0 & 0 & 0 & s_{44}/2 & 0 & 0\\ 0 & 0 & 0 & 0 & s_{44}/2 & 0\\ 0 & 0 & 0 & 0 & 0 & s_{66}/2 \end{bmatrix}\begin{Bmatrix}\sigma_{xx}\\ \sigma_{yy}\\ \sigma_{zz}\\ \sigma_{yz}\\ \sigma_{zx}\\ \sigma_{xy}\end{Bmatrix} + \begin{bmatrix} \bar{d}^{*}_{111} & \bar{d}^{*}_{211} & \bar{d}^{*}_{311}\\ \bar{d}^{*}_{122} & \bar{d}^{*}_{222} & \bar{d}^{*}_{322}\\ \bar{d}^{*}_{133} & \bar{d}^{*}_{233} & \bar{d}^{*}_{333}\\ \bar{d}^{*}_{123} & \bar{d}^{*}_{223} & \bar{d}^{*}_{323}\\ \bar{d}^{*}_{131} & \bar{d}^{*}_{231} & \bar{d}^{*}_{331}\\ \bar{d}^{*}_{112} & \bar{d}^{*}_{212} & \bar{d}^{*}_{312}\end{bmatrix}\begin{Bmatrix}E_x\\ E_y\\ E_z\end{Bmatrix}+\begin{Bmatrix}\varepsilon^{r}_{xx}\\ \varepsilon^{r}_{yy}\\ \varepsilon^{r}_{zz}\\ \varepsilon^{r}_{yz}\\ \varepsilon^{r}_{zx}\\ \varepsilon^{r}_{xy}\end{Bmatrix} \tag{21}$$

$$\begin{Bmatrix}D_x\\ D_y\\ D_z\end{Bmatrix}=\begin{bmatrix} \bar{d}^{*}_{111} & \bar{d}^{*}_{122} & \bar{d}^{*}_{133} & \bar{d}^{*}_{123} & \bar{d}^{*}_{131} & \bar{d}^{*}_{112}\\ \bar{d}^{*}_{211} & \bar{d}^{*}_{222} & \bar{d}^{*}_{233} & \bar{d}^{*}_{223} & \bar{d}^{*}_{231} & \bar{d}^{*}_{212}\\ \bar{d}^{*}_{311} & \bar{d}^{*}_{322} & \bar{d}^{*}_{333} & \bar{d}^{*}_{323} & \bar{d}^{*}_{331} & \bar{d}^{*}_{312}\end{bmatrix}\begin{Bmatrix}\sigma_{xx}\\ \sigma_{yy}\\ \sigma_{zz}\\ \sigma_{yz}\\ \sigma_{zx}\\ \sigma_{xy}\end{Bmatrix}+\begin{bmatrix} \in^{\mathrm{T}}_{11} & 0 & 0\\ 0 & \in^{\mathrm{T}}_{11} & 0\\ 0 & 0 & \in^{\mathrm{T}}_{33}\end{bmatrix}\begin{Bmatrix}E_x\\ E_y\\ E_z\end{Bmatrix}+\begin{Bmatrix}P^{r}_{x}\\ P^{r}_{y}\\ P^{r}_{z}\end{Bmatrix} \tag{22}$$

where

$$\bar{d}^{*}_{ijk}=\{\bar{d}_{33}n_in_kn_l+\bar{d}_{31}(n_i\delta_{kl}-n_in_kn_l)+\frac{1}{2}\bar{d}_{15}(\delta_{ik}n_l-2n_in_kn_l+\delta_{il}n_k)\} \tag{23}$$

In Eq. (23), n_i is the unit vector in the poling direction and δ_{ij} is the Kronecker delta.

2.4. Domain wall motion

A domain wall displacement causes changes of strain and polarization (Cao et al. 1999). For simplicity, here the applied AC electric field $E_z=E_0\exp(i\omega t)$ is parallel to the direction of spontaneous polarization P^s in one of the domains (see Fig. 3); E_0 is the AC electric field amplitude and ω is angular frequency(=$2\pi f$ where f is frequency in Hertz). The changes of the strains and polarization due to the domain wall displacement Δl (Arlt and Dederichs, 1980) can be written as

$$\begin{aligned}\Delta\varepsilon_{xx}^{*} &= \Delta s_{11}\sigma_{xx} + \Delta s_{13}\sigma_{zz} + \Delta d_{311}E_z \\ \Delta\varepsilon_{zz}^{*} &= \Delta s_{13}\sigma_{xx} + \Delta s_{33}\sigma_{zz} + \Delta d_{333}E_z \\ \Delta P_z^{*} &= \Delta d_{311}\sigma_{xx} + \Delta d_{333}\sigma_{zz} + \Delta\in_{33}^{\mathrm{T}} E_z\end{aligned} \tag{24}$$

where all terms with Δ are the contributions from the domain wall motion, and

$$\begin{aligned}\Delta s_{11} &= \frac{(\gamma^s)^2}{2lf_D}, \quad \Delta s_{13} = -\frac{(\gamma^s)^2}{2lf_D}, \quad \Delta s_{33} = \frac{(\gamma^s)^2}{2lf_D}, \\ \Delta d_{311} &= -\frac{\gamma^s P^s}{2lf_D}, \quad \Delta d_{333} = \frac{\gamma^s P^s}{2lf_D}, \quad \Delta\in_{33}^{\mathrm{T}} = \frac{(P^s)^2}{2lf_D}\end{aligned} \tag{25}$$

In Eq. (25), l is the domain width and f_D is the force constant for the domain wall motion process. The strains ε_{xx}, ε_{zz} and electric displacement D_z are given by

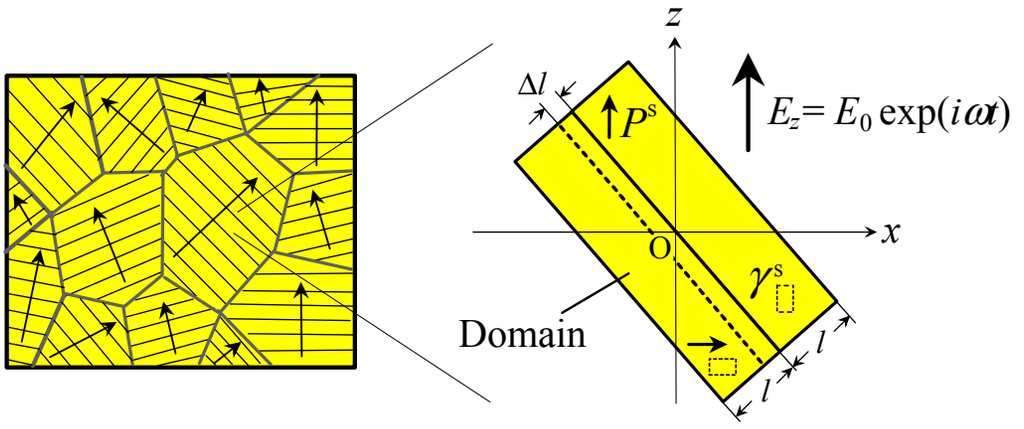

Figure 3. Schematic drawing of many grains which in turn consist of domains and basic unit of a piezoelectric crystallite with a domain wall.

$$\begin{aligned}\varepsilon_{xx} &= s_{11}^{*}\sigma_{xx} + s_{12}\sigma_{yy} + s_{13}^{*}\sigma_{zz} + d_{31}^{*}E_z \\ \varepsilon_{zz} &= s_{13}^{*}\sigma_{xx} + s_{13}^{*}\sigma_{yy} + s_{33}^{*}\sigma_{zz} + d_{31}^{*}E_z \\ D_z &= d_{31}^{*}\sigma_{xx} + d_{31}^{*}\sigma_{yy} + d_{33}^{*}\sigma_{zz} + \in_{33}^{\mathrm{T}*} E_z\end{aligned} \tag{26}$$

where

$$\begin{aligned}s_{11}^{*} &= s_{11} + \Delta s_{11}, \quad s_{13}^{*} = s_{13} + \Delta s_{13}, \quad s_{33}^{*} = s_{33} + \Delta s_{33} \\ d_{31}^{*} &= \bar{d}_{31} + \Delta d_{311}, \quad d_{33}^{*} = \bar{d}_{33} + \Delta d_{333}, \\ \in_{33}^{\mathrm{T}*} &= \in_{33}^{\mathrm{T}} + \Delta\in_{33}^{\mathrm{T}}\end{aligned} \tag{27}$$

Experimental studies on PZT ceramics have shown that 45-70% of dielectric and piezoelectric moduli values may originate from the extrinsic contributions (Luchaninov et al. 1989, Cao et al. 1991). The extrinsic dielectric constant $\Delta\in_{33}^{\mathrm{T}}$ is approximately estimated as the two thirds of the bulk properties (Li et al. 1993). Here, the following equation (Narita

et al. 2005) is utilized to describe $\Delta\in_{33}^{T}$ in terms of AC electric field amplitude E_0 and temperature dependent coercive electric field $\bar{E}_c$:

$$\Delta\in_{33}^{T}=\in_{33}^{T}\frac{2E_0}{3\bar{E}_c} \tag{28}$$

By substituting Eq. (28) into the sixth of Eq. (25), $lf_D = 3(P^s)^2\bar{E}_c/(4\in_{33}^{T}E_0)$ is obtained. By eliminating lf_D, the changes in the elastic compliances and piezoelectric coefficients in Eq. (25) can be rewritten in terms of AC electric field amplitude etc.

2.5. Finite element model

Consider a PZT stack actuator with 300 PZT layers of width W_p = 5.2 mm and thickness h_p = 0.1 mm, thin electrodes, and elastic coating layer of thickness h_e = 0.5 mm as shown in Fig. 4. A rectangular Cartesian coordinate system O-*xyz* is used and the origin of the coordinate system coincides with the center of the stack actuator. Each PZT layer is sandwiched between thin electrodes. An external electrode is attached on both sides of the actuator to address the internal electrodes.

In order to discuss the electromechanical fields near the internal electrode, the problem of the stack actuator is solved using the unit cell model (two layer piezoelectric composite with $|x| \le W_p/2 + h_e$, $|y| \le W_p/2 + h_e$, $0 \le z \le 2h_p$) shown in Fig. 5. Electrodes of length a and width W_p = 5.2 mm are attached to the PZT layer of thickness h_p = 0.1 mm, and a W_p - a tab region exists on both sides of the layer. Because of the geometric and loading symmetry, only the half needs to be analyzed. The electrode layers are not incorporated into the model.

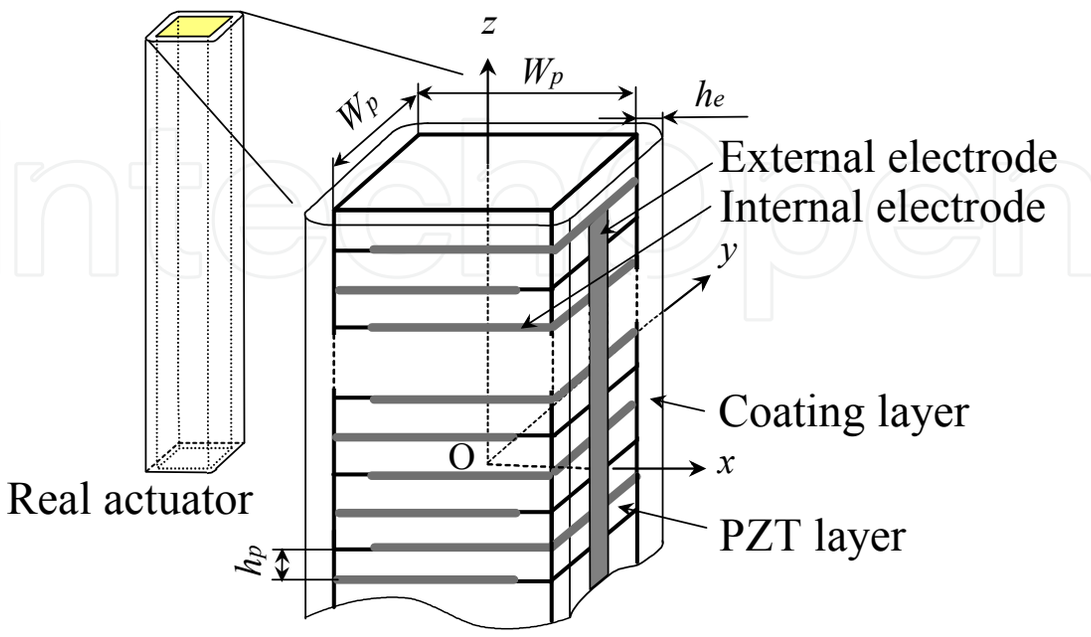

Figure 4. Schematic drawing of PZT stack actuator.

First, we consider the PZT stack actuator under DC electric fields. The electric potential on two electrode surfaces ($-W_p/2 \le x \le -W_p/2+a$, $0 \le y \le W_p/2$, $z = 0$, $2h_p$) equals the applied voltage, $\phi = V_0$. The electrode surface ($W_p/2-a \le x \le W_p/2$, $0 \le y \le W_p/2$, $z = h_p$) is connected to the ground, so that $\phi = 0$. The mechanical boundary conditions include the traction-free conditions on the coating layer surfaces at $x = \pm (W_p/2 + h_e)$, $y = W_p/2 + h_e$ and the symmetry conditions on the xz plane at $y = 0$ and xy planes at $z = 0$, $2h_p$. In addition, the origin is constrained against the displacement in the x-direction, to avoid rigid body motion. We next consider the PZT stack actuator under AC electric fields. The electric potential on two electrode surfaces ($-W_p/2 \le x \le -W_p/2+a$, $0 \le y \le W_p/2$, $z = 0$, $2h_p$) equals the applied voltage, $\phi = V_0 \exp(i\omega t)$, and the electrode surface ($W_p/2-a \le x \le W_p/2$, $0 \le y \le W_p/2$, $z = h_p$) is connected to the ground.

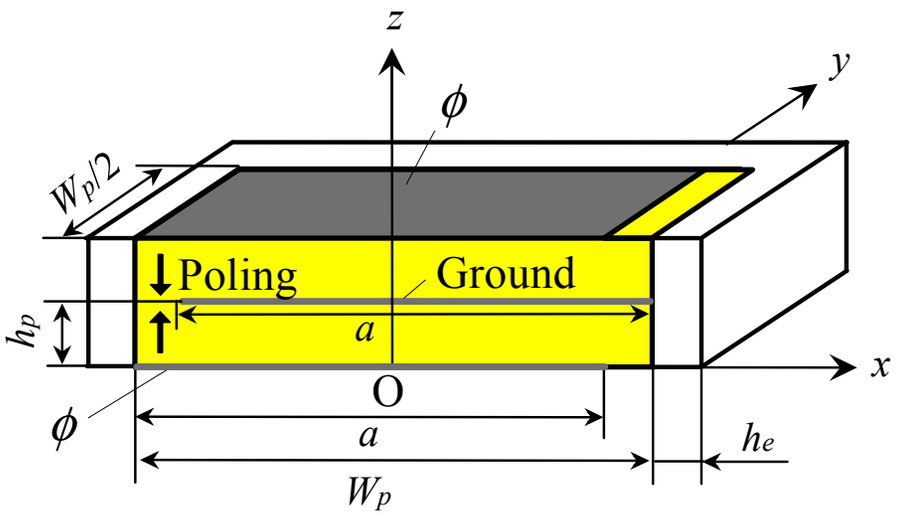

Figure 5. Unit cell of the PZT stack actuator.

Each element in ANSYS is defined by eight-node 3-D coupled field solid for the PZT layers and eight-node 3-D structural solid for the coating layer. $P^s = 0.3$ C/m^2 and $\gamma^* = 0.004$ are used. In order to calculate the electromechanical fields, we need the temperature dependent coercive electric field $\overline{E}_c$. First-principles free energy calculations for ferroelectric perovskites (Kumar and Waghmare 2010) have shown that the domain wall energy increases linearly about 50% as the temperature T decreases from room temperature to 260 K. Since higher domain wall energy leads to higher coercive electric field, the temperature dependent coercive electric field is assumed to be the following equation:

$$\overline{E}_c = (4.84 - 0.0129T)E_c \tag{29}$$

where E_c is a coercive electric field at 298 K.

3. Experiment

The stack actuator is fabricated using 300 soft PZT N-10 layers (NEC/Tokin Co. Ltd., Japan) of width $W_p = 5.2$ mm and thickness $h_p = 0.1$ mm (see Fig. 6). A rectangular Cartesian

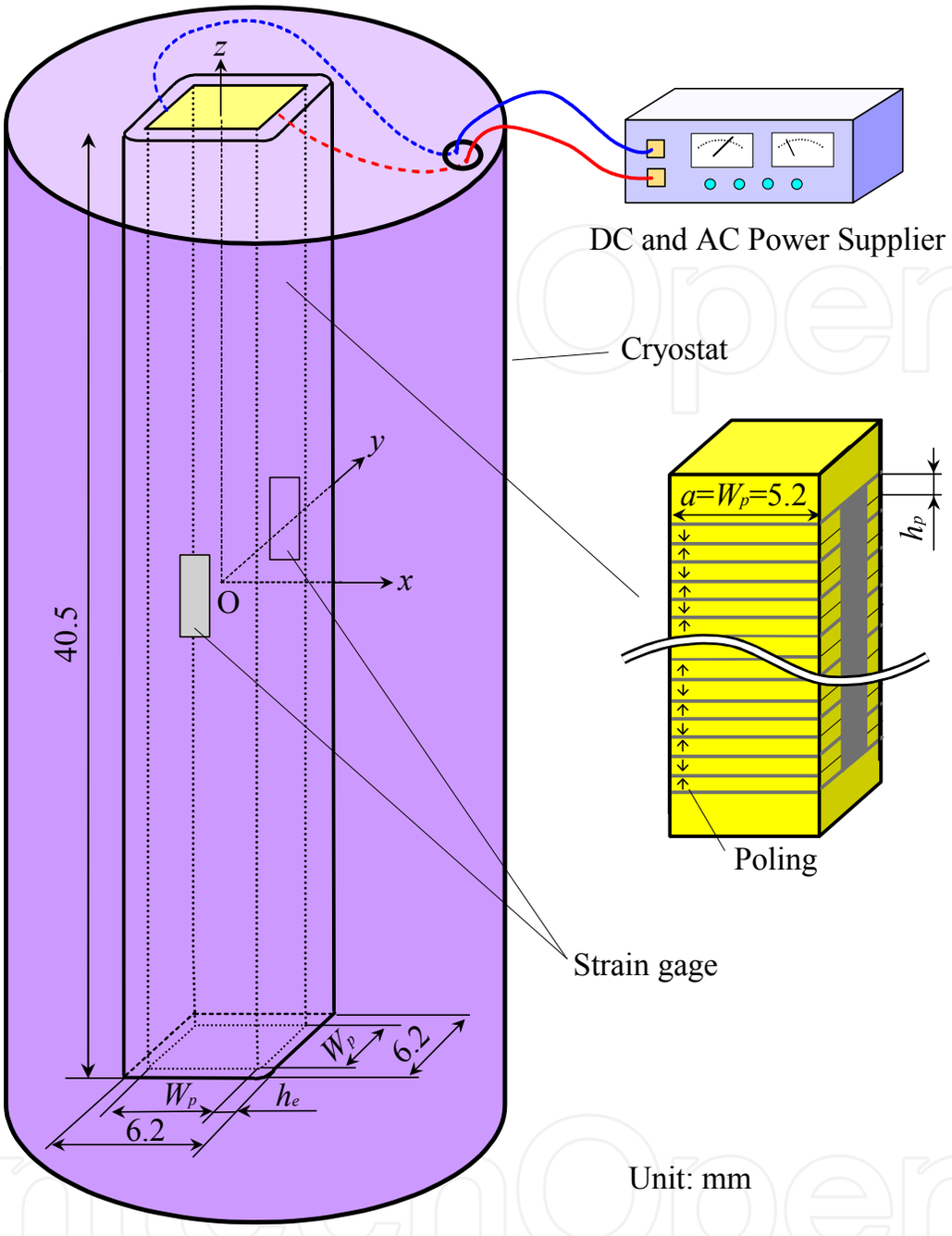

Figure 6. Experimental setup.

Elastic compliance (×10^{-12} m^2/N)					Piezoelectric coefficient (×10^{-12} m/V)			Dielectric constant (×10^{-10} C/Vm)		Density (kg/m^3)
s_{11}	s_{33}	s_{44}	s_{12}	s_{13}	d_{31}	d_{33}	d_{15}	ϵ_{11}^T	ϵ_{33}^T	ρ
14.8	18.1	44.9	-5.1	-5.8	-287	635	930	443	481	8000

Table 1. Material properties of N-10.

coordinate system O-*xyz* is used and the origin of the coordinate system coincides with the center of the actuator. The electrode length is $a = W_p = 5.2$ mm (full electrodes), and the

actuator is coated with epoxy layer of thickness h_e = 0.5 mm. The total dimensions of the specimen are width of 6.2 mm and length of 40.5 mm. Table 1 lists the material properties of N-10. The coercive electric field of N-10 at room temperature is approximately E_c = 0.36 MV/m. Young's modulus, Poisson's ratio and mass density of epoxy layer are 3.35 GPa, 0.214 and 1100 kg/m^3, respectively.

The actuator is bonded to the test rig of a SUS304 stainless steel plate using epoxy bond, and DC voltage (0 Hz) and AC voltage (400 Hz) are applied using a power supply. Two strain gages are attached at the center of the $y = \pm 3.1$ mm planes, and the magnitude of strain is measured. To control the temperature of the actuator, an automated helium refill system (TRG-300, Taiyo Toyo Sanso Co. Ltd., Japan) is used. For the reliability of the test, two specimens are experimented, and four strain values are obtained.

4. Results and discussion

We first consider the PZT stack actuators under DC electric fields. Figure 7 shows the predicted normal strain ε_{zz} versus temperature T at x = 0 mm, $y = W_p/2 + h_e$ = 3.1 mm and z = 0 mm of the PZT stack actuators for mole fraction X = 0.44 and 0.56 with $a = W_p$ = 5.2 mm (full electrodes) under DC electric field $E_0 = V_0/h_p$ = 0.1 MV/m (f = 0 Hz). Also shown are the measured data (average of four values) for X = 0.44. The electric field induced stain of the PZT stack actuator for X = 0.44 decreases with decreasing temperature due to a shift in the MPB. We see that the trend is sufficiently similar between the prediction and measurement. On the other hand, the electric field induced stain of the PZT stack actuator for X = 0.56 tends to increase with decreasing temperature reaching a peak at about T = 20 K and then decrease in magnitude. Figure 8 shows the predicted normal strain ε_{zz} versus DC electric field E_0 at x = 0 mm, y = 3.1 mm and z = 0 mm (strain measurement location) of the PZT stack actuators for X = 0.56 with a = 5.0 mm (partial electrodes) and $a = W_p$ = 5.2 (full electrodes) at liquid hydrogen temperature (20 K). Strain versus electric field curves show nonlinear behavior due to the polarization switching under high negative DC electric fields. Small difference is observed in the DC electric field induced strains for a = 5.0 and 5.2 mm. Figure 9 shows the polarization switching zones near the electrode tip (x = 2.4 mm) at y = 0 mm plane of the PZT layer for X = 0.56 with a = 5.0 mm (partial electrodes) at 20 K. The coercive electric field at 20 K is about 1.65 MV/m. As the negative DC electric field increases, the area of the switched region grows.

We next consider the PZT stack actuators under AC electric fields. Figure 10 shows the normal strain ε_{zz} versus electric field amplitude E_0 at x = 0 mm, y = 3.1 mm and z = 0 mm of the PZT stack actuators for X = 0.44 and 0.56 at frequency f = 400 Hz and T = 20 K. The dashed line represents the strain computed by the FEA without domain wall motion effect, and the solid line represents the strain after the domain wall motion effect has been applied. The open circle denotes the experimental data. As AC electric field increases, the strain increases gradually away from the linear curve. This is due to the domain wall motion under the influence of AC electric fields. It can be seen that agreement between analysis

with domain wall motion effect and experiment is fair. Figure 11 shows the distribution of the normal component of stress σ_{zz} as a function of x at y = 0 mm and z = 0.025 mm of the PZT stack actuators for X = 0.44 and 0.56 with a = 5.0 mm (partial electrodes) and $a = W_p$ = 5.2 mm (full electrodes) under E_0 = 1.65 MV/m at f = 400 Hz and 20 K. The coercive electric field at 20 K is about 1.65 MV/m. In the case of the PZT stack actuator with full electrodes, small difference is observed for X = 0.44 and 0.56. For the PZT stack actuators with partial electrodes, a high normal stress occurs near the electrode tip (x = 2.4 mm) as is expected. Figure 12 shows the electric field distribution E_z as a function of x at y = 0 mm and z = 0.025 mm for the PZT stack actuators with a = 5.0 mm (partial electrodes) and a = 5.2 mm (full electrodes) under E_0 = 1.65 MV/m at f = 400 Hz and 20 K. For the PZT stack actuators with partial electrodes, a high electric field is observed near the electrode tip.

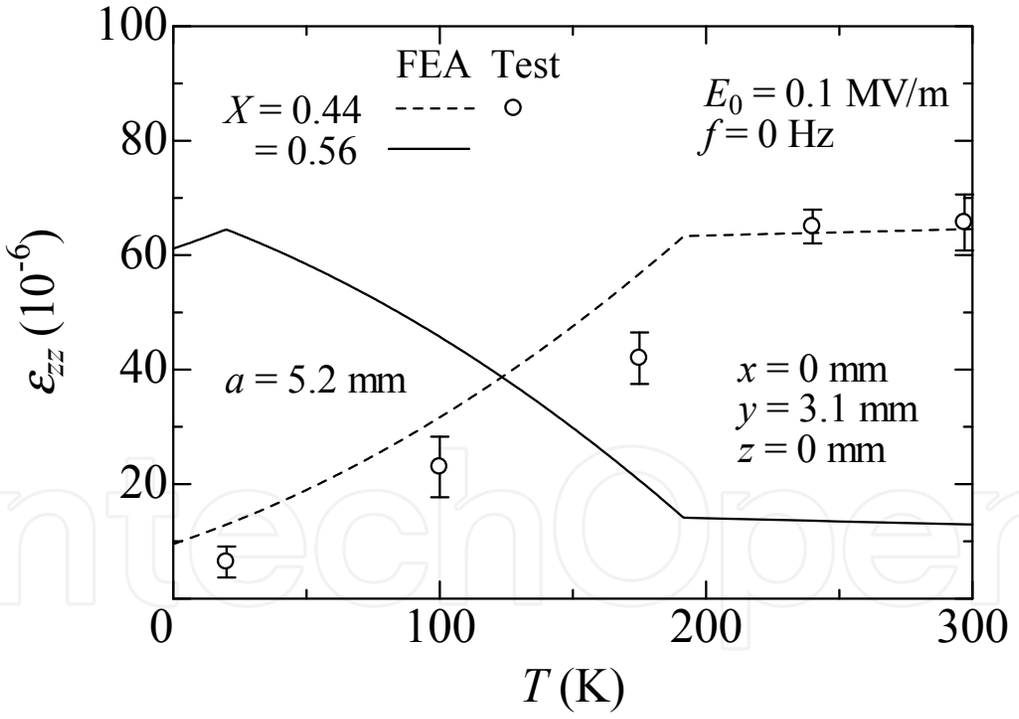

Figure 7. Strain vs temperature of PZT stack actuators for X = 0.44 and 0.56 under DC electric field E_0 = 0.1 MV/m.

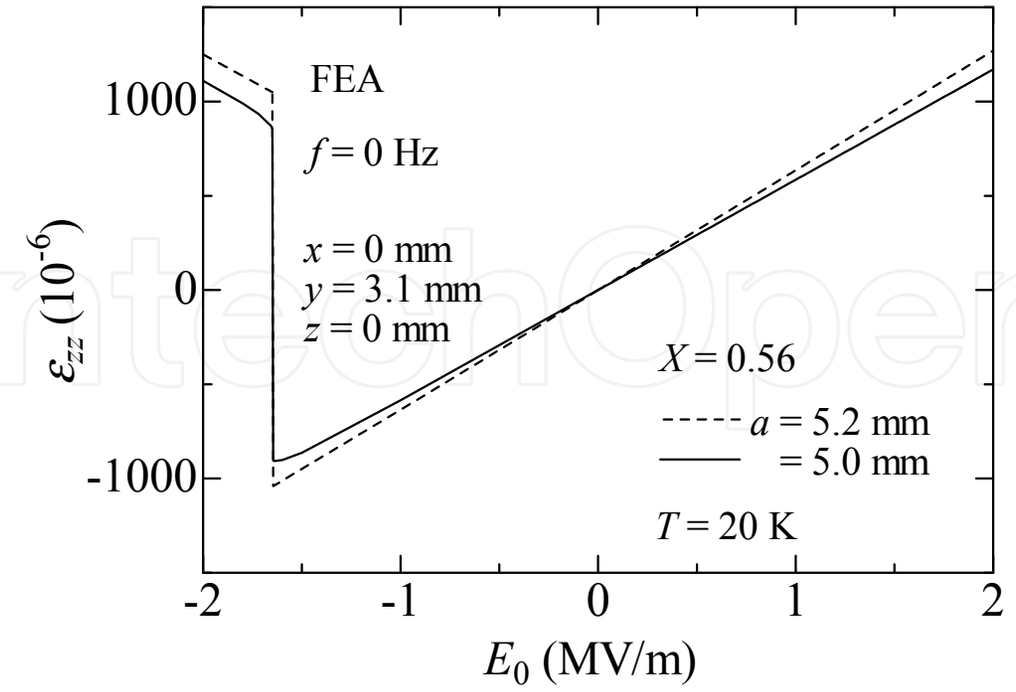

Figure 8. Strain vs DC electric field of PZT stack actuators for X = 0.56 at 20 K.

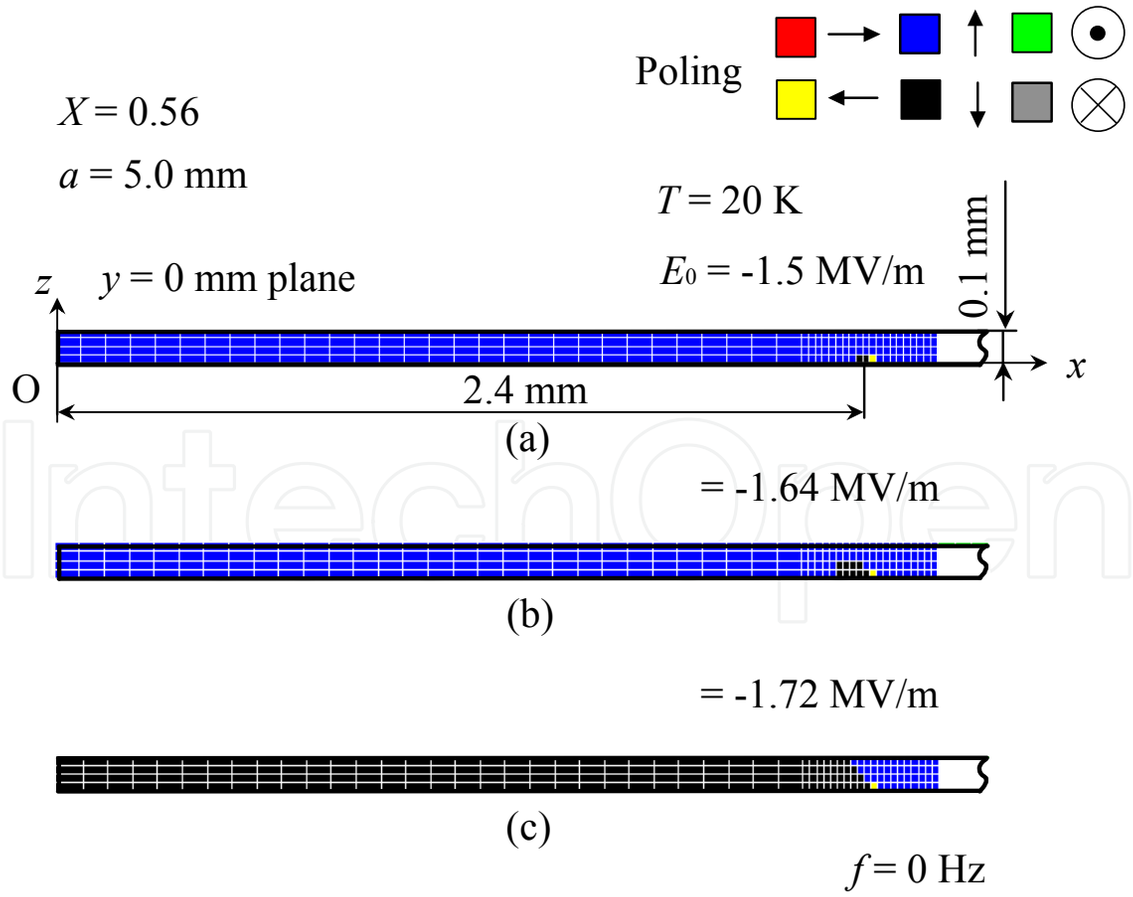

Figure 9. Polarization switching zones at y = 0 mm plane of PZT layer for X = 0.56 at 20 K, induced by DC electric field (a) E_0 = -1.5 MV/m, (b) E_0 = -1.64 MV/m and (c) E_0 = -1.72 MV/m.

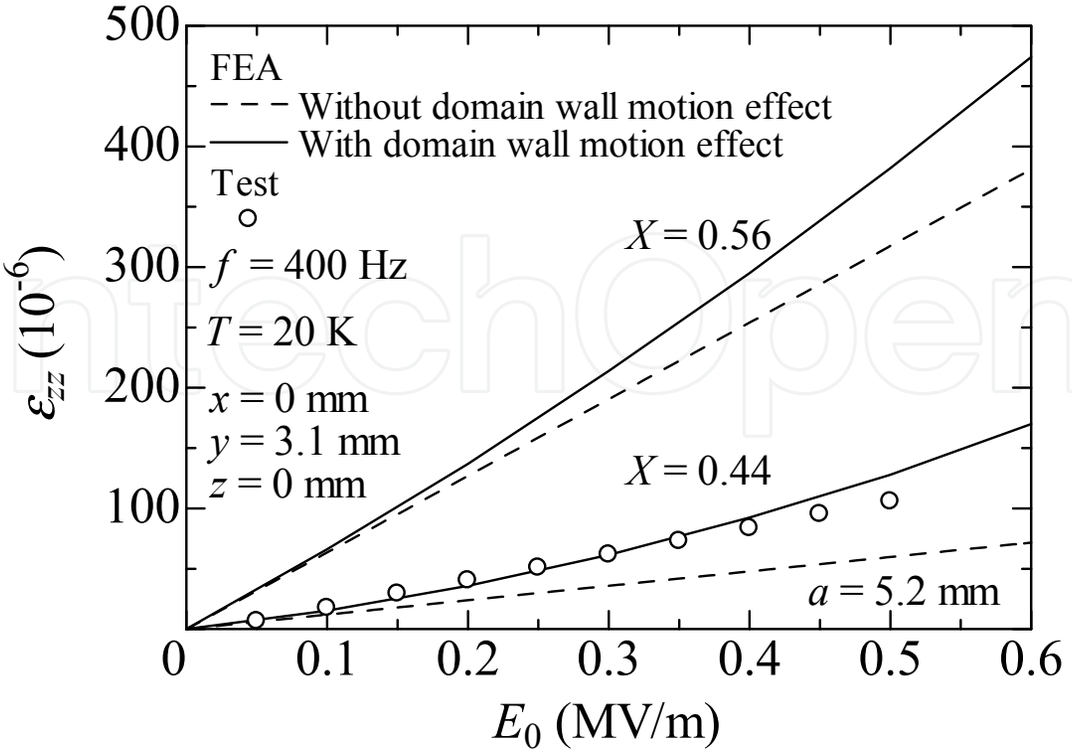

Figure 10. Strain vs AC electric field of PZT stack actuators for X = 0.44 and 0.56 at 20 K.

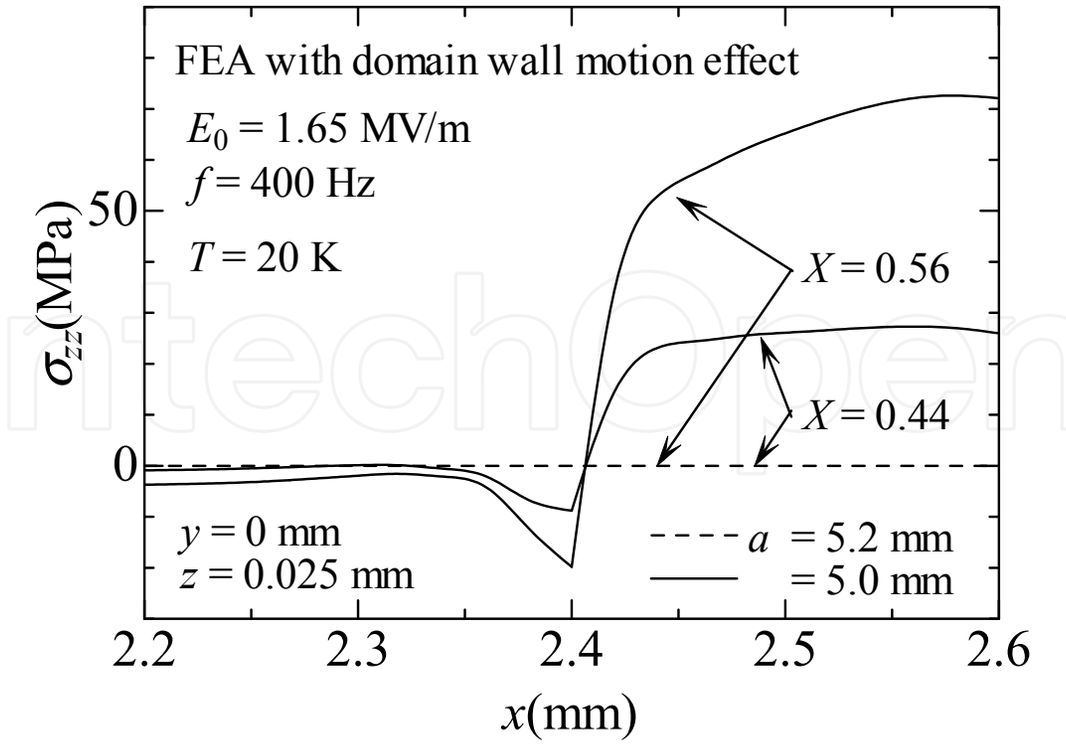

Figure 11. Variation of normal stress σ_{zz} as a function of x at y = 0 mm and z = 0.025 mm for PZT stack actuators under AC electric field E_0 = 1.65 MV/m at T = 20 K.

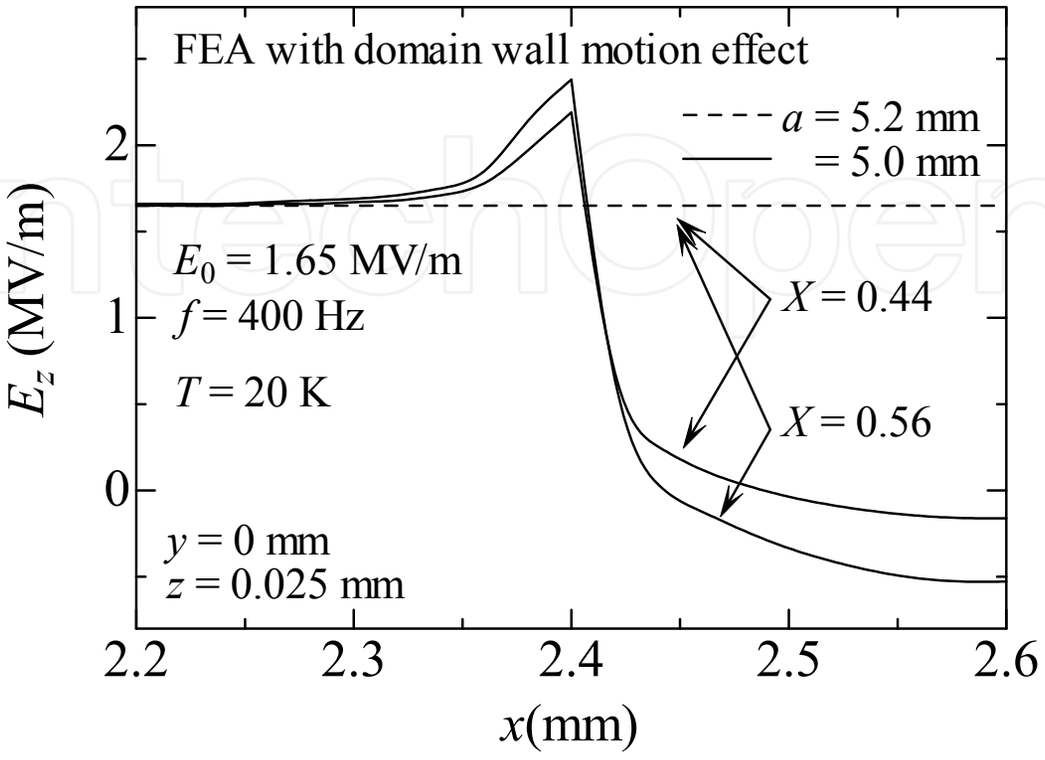

Figure 12. Variation of electric field E_z as a function of x at y = 0 mm and z = 0.025 mm for PZT stack actuators under E_0 = 1.65 MV/m at T = 20 K.

5. Conclusions

Numerical and experimental examination on the electromechanical response of PZT stack actuators at cryogenic temperatures is reported. It is found that the electric field induced strain decreases or increases with decreasing temperature depending on the mole fraction. That is, in the case of high performance PZTs for X = 0.44, the electric field induced strain is very high at room temperature, whereas in the case of PZTs for X = 0.56, the electric field induced strain at cryogenic temperatures will seem to be higher than at room temperature. It is also shown that the stress and electric field in the PZT layers are very high near the electrode tip for the PZT stack actuators with partial electrodes, although the electric field induced strains at the center of the surface for the partially and fully electroded PZT stack actuators have the same level. This study may be useful in designing high performance hydrogen fuel injectors.

Author details

Yasuhide Shindo and Fumio Narita
Tohoku University, Japan

6. References

Arlt, G. & Dederichs, H. (1980). Complex elastic, dielectric and piezoelectric constants by domain wall damping in ferroelectric ceramics, *Ferroelectrics*, Vol. 19: 47-50.

Bell, A. J. & Furman, E. (2003). A two-parameter thermodynamic model for PZT, *Ferroelectrics* Vol. 293: 19-31.

Boucher, E., Guiffard, B., Lebrum, L. & Guyomar, D. (2006). Effects of Zr/Ti ratio on structural, dielectric and piezoelectric properties of Mn- and (Mn, F)-doped lead zirconate titanate ceramics, *Ceramics International* Vol. 32 (No. 5): 479-485.

Cao, S., Li, W. and Cross, L. E. (1991). The extrinsic nature of nonlinear behavior observed in lead zirconate titanate ferroelectric ceramic, *Journal of Applied Physics*, Vol. 69: 7219-7224.

Hwang, S.C., Lynch, C.S. & McMeeking, R.M. (1995). Ferroelectric/ferroelastic interactions and a polarization switching model, *Acta Metallurgica et Materialia*, Vol. 43 (No. 5): 2073-2084.

Jaffe, B., Cook, W. R. & Jahhe, H. (1971). *Piezoelectric Ceramics*, Academic, New York.

Kumar, A. & Waghmare, U. V. (2010). First-principles free energies and Ginzburg-Landau theory of domains and ferroelectric phase transitions in $BaTiO_3$, *Physical Review B*, Vol. 82: 054117.

Li, S., Bhalla, A. S., Newnham, R. E. & Cross, L. E. (1993). Quantitative evaluation of extrinsic contribution to piezoelectric coefficient d_{33} in ferroelectric PZT ceramics, *Materials Letter*, Vol. 17: 21-26.

Luchaninov, A. G., Shil'nikov, A. V., Shuvalov, L. A. & Shipkova, I. J. U. (1989). The domain processes and piezoeffect in polycrystalline ferroelectrics, *Ferroelectrics*, Vol. 98: 123-126.

Narita, F., Shindo, Y. & Mikami, M. (2005). Analytical and experimental study of nonlinear bending response and domain wall motion in piezoelectric laminated actuators under AC electric fields, *Acta Materialia*, Vol. 53 (No. 17): 4523-4529.

Noheda, B., Cox, D. E., Shirane, G., Guo, R., Jones, B. & Cross, L. E. (2000). Stability of the monoclinic phase in the ferroelectric perovskite $PbZr_{1-x}Ti_xO_3$, *Physical Review B* Vol. 63 (No. 1): 014103.

Pandey, D., Singh, A. K. & Baik, S. (2008). Stability of ferroic phases in the highly piezoelectric $Pb(Zr_xTi_{1-x})O_3$ ceramics, *Acta Crystallographica Section A* Vol. 64: 192-203.

Senousy, M. S., Li, F. X., Mumford, D., Gadala, M. & Rajapakse, R. K. N. D. (2009a). Thermo-electro-mechanical performance of piezoelectric stack actuators for fuel injector applications, *Journal of Intelligent Material Systems and Structures* Vol. 20: 387-399.

Senousy, M. S., Rajapakse, R. K. N. D., Mumford D. & Gadala, M. S. (2009b). Self-heat generation in piezoelectric stack actuators used in fuel injectors, *Smart Materials and Structures* Vol. 18: 045008.

Shindo, Y., Narita, F. & Sasakura, T. (2011). Cryogenic electromechanical behavior of multilayer piezo-actuators for fuel injector applications, *Journal of Applied Physics* Vol. 110 (No. 8): 084510.

Shindo, Y., Sasakura, T. & Narita, F. (2012). Dynamic electromechanical response of multilayered piezoelectric composites from room to cryogenic temperatures for fuel injector applications, *ASME Journal of Engineering Materials and Technology*, in press.

IntechOpen